



## Influence of trapped thermal particles on internal kink modes in high temperature tokamaks

T. M. Antonsen Jr. and Anders Bondeson

Citation: *Physics of Fluids B: Plasma Physics (1989-1993)* **5**, 4090 (1993); doi: 10.1063/1.860577

View online: <http://dx.doi.org/10.1063/1.860577>

View Table of Contents: <http://scitation.aip.org/content/aip/journal/pofb/5/11?ver=pdfcov>

Published by the [AIP Publishing](#)

---

### Articles you may be interested in

[Effects of energetic trapped electrons on the internal kink instability in tokamaks](#)

*AIP Conf. Proc.* **595**, 334 (2001); 10.1063/1.1424204

[Alpha particle effects on the internal kink and fishbone modes](#)

*Phys. Plasmas* **1**, 3369 (1994); 10.1063/1.870485

[Nonlinear evolution of the internal kink mode in toroidal geometry for shaped tokamak plasmas](#)

*Phys. Fluids* **31**, 1202 (1988); 10.1063/1.866749

[Influence of resistivity on energetic trapped particle-induced internal kink modes](#)

*Phys. Fluids* **29**, 1760 (1986); 10.1063/1.865652

[Trapped particle destabilization of the internal kink mode](#)

*Phys. Fluids* **28**, 278 (1985); 10.1063/1.865198

---

# Influence of trapped thermal particles on internal kink modes in high temperature tokamaks

T. M. Antonsen, Jr.<sup>a)</sup> and Anders Bondeson

*Centre de Recherches en Physique des Plasmas, Association Euratom-Confédération Suisse, Ecole Polytechnique Fédérale de Lausanne, 21, Av. des Bains, CH-1007 Lausanne, Switzerland*

(Received 18 June 1993; accepted 30 July 1993)

The effects of thermal trapped particles on the  $n=1$  internal kink mode are studied using drift kinetic theory. Strong modifications of the magnetohydrodynamic (MHD) results are found, and marginal stability generally occurs at nonzero rotation frequency. For equal electron and ion temperatures, the trapped particles increase the marginal poloidal beta at  $q=1$  substantially above the MHD value. For unequal electron and ion temperatures, the drift resonance with the hotter species becomes increasingly destabilizing and for sufficiently unequal temperatures, this leads to instability below the ideal-MHD threshold. Treatment of trapped thermal particles requires consideration of the effects of an electrostatic potential. The potential is weakly stabilizing for the internal kink mode. Furthermore, finite beta couples unstable, nearly electrostatic, trapped particle modes to the internal kink mode. At high beta, thermal fluctuations of the trapped particle modes can lead to significant internal kink displacements.

## I. INTRODUCTION

The central region of tokamaks is often subject to the so-called sawtooth oscillations with periodic redistributions of the thermal energy and magnetic flux. The trigger of these relaxations is the internal  $n=1$  kink mode (where  $n$  is the toroidal mode number). This mode gives a nearly rigid shift of the internal region of the plasma. Its suppression or control is considered to be important in present and future tokamaks. In its ideal and most robust form, to which we restrict attention here, it grows on the time scale over which the plasma is ideally conducting.

It is well known that the stability of the internal kink mode in tokamaks can be strongly influenced by energetic, magnetically trapped particles.<sup>1-5</sup> The purpose of the present article is to show that also the *thermal* trapped particles significantly change the stability boundaries of the ideal internal kink. A simple estimate of this effect, based on the low frequency kinetic energy principle,<sup>6-8</sup> proceeds as follows. For a large aspect ratio circular tokamak, the potential energy for an internal kink from ideal magnetohydrodynamic (MHD) theory<sup>9</sup> in the absence of kinetic effects is

$$\Delta W_{\text{MHD}} \approx c_{\text{MHD}} \varepsilon_{q=1}^4 (\beta_{pc}^2 - \beta_p^2) \xi^2 R_0 B_0^2, \quad (1)$$

where  $\varepsilon_{q=1}$  is the inverse aspect ratio of the  $q=1$  surface,  $\xi$  the displacement of the central region,  $R_0$  the major radius of the torus, and  $B_0$  is the strength of the confining magnetic field. Furthermore,  $c_{\text{MHD}}$  is a profile dependent coefficient,  $\beta_p$  is the poloidal beta evaluated at the  $q=1$  surface, and  $\beta_{pc}$  is the critical value of  $\beta_p$  required for ideal MHD instability. Typically,  $\beta_{pc}$  is in the range of 0.1 to 0.2 for plasmas with rounded current profiles and circular cross section,<sup>9</sup> but it can be much lower when the shear is weak

and/or the cross section is elliptic.<sup>10</sup> The coefficient  $c_{\text{MHD}}$  is proportional to the central shear (that is, to  $1-q_0$ ). Using the low frequency energy principle<sup>6-8</sup> the contribution of magnetically trapped thermal particles can be estimated as

$$\Delta W_{\text{trapped}} \approx c_{\text{LF}} \varepsilon_{q=1}^2 \varepsilon_{q=1}^{1/2} (\varepsilon_{q=1} \beta_p) \xi^2 R_0 B_0^2. \quad (2)$$

The numerical coefficient  $c_{\text{LF}}$  represents integrations over distribution functions and profiles. (The large aspect ratio calculation in the Appendix gives  $c_{\text{LF}} \approx \sqrt{2}/7 \approx 0.20$  assuming a parabolic pressure profile which gives a  $4\pi p_0 = B_0^2 \varepsilon_a^2 \beta_p$  where  $\varepsilon_a = a/R$  is the inverse aspect ratio of the torus.) The factor  $\varepsilon_{q=1}^2$  results from the assumption that the displacement is confined to the region inside the  $q=1$  surface,  $\varepsilon_{q=1}^{1/2}$  is the fraction of particles which are trapped and experience the unfavorable curvature of the toroidal field, and  $\varepsilon_{q=1} \beta_p$  represents the pressure gradient at the  $q=1$  surface. It should be noted that the trapped thermal particles contribute to both  $\Delta W_{\text{MHD}}$  and  $\Delta W_{\text{trapped}}$ . Their contribution to  $\Delta W_{\text{MHD}}$  is destabilizing but is nearly cancelled by their contribution to  $\Delta W_{\text{trapped}}$ . The net result appears to be stabilizing since only the circulating particles, which experience predominantly favorable curvature contribute to the potential energy.

Combining the above estimates, the condition for ideal instability, including the effects of trapped particles, becomes

$$\beta_p^2 - (c_{\text{LF}}/c_{\text{MHD}}) \varepsilon_{q=1}^{-1/2} \beta_p > \beta_{pc}^2. \quad (3)$$

As  $\beta_{pc}$  is typically well below  $(c_{\text{LF}}/c_{\text{MHD}}) \varepsilon_{q=1}^{-1/2}$ , the thermal trapped particles have a strong stabilizing effect on the  $n=1$  internal kink, in particular when  $1-q_0$  is small. This may resolve the apparent contradiction between experimental observations of  $q_0$  below unity during the entire sawtooth cycle,<sup>11</sup> and the results of fluid theories which predict a rather unstable behavior when  $q_0 < 1$ . Notably, fluid simulations generally lead to complete reconnection in accordance with the Kadomtsev model<sup>12</sup> and resistive-

<sup>a)</sup>Permanent address: Departments of Electrical Engineering and Physics and Laboratory for Plasma Research, University of Maryland, College Park, Maryland 20742.

MHD analysis<sup>13</sup> shows that most profiles with  $q_0 < 1$  are linearly unstable. The stabilization by thermal trapped particles has been considered previously by Hastie and Hender<sup>14</sup> using the Kruskal–Oberman<sup>15</sup> or “high frequency” energy principle. Here, we consider the case where the mode frequency is comparable to the drift frequencies and apply drift kinetic theory.<sup>6–8</sup>

The stabilizing influence of the trapped particles results from their inability to respond to flutelike perturbations which develop slowly compared with the time it takes for the particles to drift around the torus. Since the trapped particles spend most of their time in the region of unfavorable magnetic curvature, eliminating their contribution to the perturbed potential energy can be strongly stabilizing.<sup>1</sup> This holds, in particular, for the  $n=1$  internal kink which is driven by the average curvature and has  $\Delta W_{\text{MHD}} = O(\epsilon_{q=1}^4)$ , as opposed to strongly ballooning modes, which localize in the bad curvature region and have  $\Delta W_{\text{MHD}} = O(\epsilon^3)$ . If the trapped particle contribution is removed from a mode sensitive to the average curvature, the remaining effect from the passing particles can be stabilizing, as shown by Eq. (3) when  $\beta_p < (c_{\text{LF}}/c_{\text{MHD}})\epsilon_{q=1}^{-1/2}$ . Similar remarks apply to Mercier modes, which are strongly affected by trapped particle effects.<sup>6,16</sup> However, because the trapped particles experience unfavorable curvature, this form of stabilization is not robust. (The low frequency energy principle gives neither necessary nor sufficient stability criteria in this case.<sup>6,7</sup>) Indeed, a plasma with energetic ions is still susceptible to a perturbation which develops on the time scale of the toroidal drift frequency. This type of instability is responsible for the “fishbone” oscillations observed in some tokamaks with neutral injection.<sup>1</sup> We will show that such drift resonances play an important role for the thermal trapped particles. However, when the temperatures of the trapped electrons and ions, whose toroidal drifts are in opposite directions, are nearly equal, the plasma is less susceptible to fishbone instabilities.

The present calculation is ideal, but an important motivation for it originally came from resistive MHD. Linear resistive MHD computations<sup>13</sup> give extremely restrictive conditions for the stability of the internal kink mode. However, experimentally, large scale instability is observed only just before a sawtooth crash, and it is thought that  $q_0$  remains below unity for most of the sawtooth cycle. There are many indications that the resistive-MHD stability thresholds are too restrictive, e.g., by comparison with the experimentally observed values of the poloidal beta at  $q=1$ . As will be shown here, thermal trapped particles are strongly stabilizing for the internal kink mode, and this stabilization may help bring resistive-MHD (and other nonideal) theories in better agreement with the experimental results.

## II. FORMULATION

To study the effects of thermal trapped particles on ideal  $n=1$  modes, we have extended the toroidal, resistive-MHD code MARS<sup>17</sup> to include trapped particles. The present version applies bounce-averaged drift kinetic theory<sup>7</sup> for the trapped particles combined with ideal

MHD and an electrostatic potential. The model thus includes interaction between internal kink modes and electrostatic trapped particle modes. We consider perturbations which are “quasi ideal,” including the parallel electric field, generated by the scalar potential, but magnetic reconnection is excluded. The parallel electric field is required to maintain quasineutrality in the presence of the perturbed density of trapped particles. The perturbed electric field is expressed in terms of a displacement (perpendicular to the equilibrium magnetic field) and the electrostatic potential  $\Phi$

$$\mathbf{E} = \frac{i\omega}{c} \xi \times \mathbf{B} - \nabla \Phi. \quad (4)$$

The bounce-averaged drift kinetic equation leads to the following quadratic form:<sup>7</sup>

$$\Delta W_T(\xi^*, \xi, \Phi^*, \Phi) = K + \Delta W_f + \Delta W_\Phi + \Delta W_k = 0 \quad (5)$$

from which the Euler equations determining  $\Phi$  and the two components of  $\xi$  are obtained by taking variations with respect to the conjugate quantities. The quantities appearing  $\Delta W_T$  are defined as follows. The kinetic energy is

$$K = -\frac{1}{2}\omega^2 \int d^3x \rho_m \xi^* \cdot \left( \xi + \frac{ic}{\omega B} \mathbf{b} \times \nabla \Phi \right), \quad (6)$$

where  $\rho_m$  is the mass density. The “fluid” contribution to the potential energy is

$$\begin{aligned} \Delta W_f = \frac{1}{2} \int d^3x & \left[ \frac{1}{4\pi} |\mathbf{Q} \times \mathbf{b}|^2 \right. \\ & + \left| \mathbf{Q} \cdot \mathbf{b} - \frac{4\pi}{B} \xi^* \cdot \nabla p \right|^2 \xi^* \cdot \mathbf{Q} \times \mathbf{b} \mathbf{b} \cdot \nabla \times \mathbf{B} \\ & \left. - 2\xi^* \cdot \kappa \xi \cdot \nabla p \right], \end{aligned} \quad (7)$$

where  $\mathbf{Q} = \nabla \times (\xi \times \mathbf{B})$  is the perturbed magnetic field. The adiabatic contribution from the electrostatic potential is given by

$$\Delta W_\Phi = \frac{1}{2} \int d^3x \rho_\Phi |\Phi|^2, \quad (8a)$$

where

$$\rho_\Phi = \sum_j q_j^2 \int d\Gamma \frac{\partial f_{0j}}{\partial \epsilon} = - \sum_j q_j^2 n_j / T_j. \quad (8b)$$

The second equality in Eq. (8b) applies for a Maxwellian plasma, which we will assume throughout. Furthermore,  $q_j$ ,  $n_j$ , and  $T_j$  denote the charge, number density, and temperature of species  $j$ . The kinetic contribution to the potential energy is

$$\Delta W_k = -\frac{1}{2} \int d^3x \sum_j \left\langle \left\langle \int_{\text{trapped}} d\Gamma \frac{Df_{0j}}{D\epsilon} |H|^2 \right\rangle \right\rangle, \quad (9a)$$

where we introduced the notation

$$\frac{Df_{0j}}{D\varepsilon} = \frac{\omega \partial f_{0j} / \partial \varepsilon - (nc/q_j) \partial f_{0j} / \partial \psi}{\omega - \langle \omega_{dj} \rangle + i\nu_{\text{eff}}} \\ = -\frac{f_{0j}}{T_j} \frac{\omega - \omega_{*j} [1 + \eta_j (\varepsilon/T_j - 3/2)]}{\omega - \langle \omega_{dj} \rangle + i\nu_{\text{eff}}} \quad (9b)$$

and the second equality again assumes Maxwellian distributions. Single brackets denote the bounce average for trapped particles  $\langle \cdot \rangle = (\int \cdot dl/v_{\parallel}) / (\int dl/v_{\parallel})$ . Double brackets imply an average over the poloidal angle  $\chi$ ,  $\langle\langle \cdot \rangle\rangle = \int \cdot J d\chi / \int J d\chi$  which is used to turn a poloidal integration into an orbital integral.  $J$  is the Jacobian from flux coordinates  $(\psi, \chi, \phi)$  to real space. The integration element in velocity space is

$$d\Gamma = \sum_{\pm} \frac{2\pi B}{m} \frac{\sigma(\varepsilon - \mu B) d\varepsilon d\mu}{\sqrt{2m(\varepsilon - \mu B)}}, \quad (10)$$

where  $\sigma$  is the Heaviside function,  $\varepsilon = mv^2/2$ , and  $\mu = mv_{\parallel}^2/2B$ . The perturbed energy  $H$  is defined as

$$H = \langle [\mu(\mathbf{Q} \cdot \mathbf{b} + \xi \cdot \nabla B) + mv_{\parallel}^2 \xi \cdot \kappa + q\Phi] \\ \times \exp[in\phi(\chi)] \rangle, \quad (11)$$

where the exponential factor accounts for the toroidal variation along the field lines and  $\kappa = \mathbf{b} \cdot \nabla \mathbf{b}$ . If the equilibrium magnetic field is represented as  $\mathbf{B} = \nabla \alpha \times \nabla \psi$  with  $\alpha = \phi - \int \chi q_l d\chi'$ , then  $\phi(\chi) = \int \chi q_l d\chi'$ . The diamagnetic and curvature drift frequencies are

$$\omega_{*j} = -n \frac{cT_j}{q_j n_j} \frac{\partial n_j}{\partial \psi}, \quad \langle \omega_{dj} \rangle = n \langle \mathbf{v}_{dj} \cdot \nabla \alpha \rangle, \quad (12)$$

where  $\mathbf{v}_{dj} = (cb/q_j B) \times (m_j v_{\parallel}^2 \kappa + \mu \nabla B)$  is the magnetic drift velocity. The strength of the temperature gradient is measured by  $\eta_j = d(\ln T_j)/d(\ln n_j)$ , and  $\nu_{\text{eff}}$  is an effective detrapping rate due to collisions.

Our model includes drift and diamagnetic effects for the trapped particles, but not for the circulating particles. The diamagnetic drift of circulating ions can be important in the small inertial layer in the vicinity of the  $q=1$  rational surface. This is the effect which is responsible for the usual finite Larmor radius stabilization of MHD instabilities. This stabilization, however, is defeated by the collisionless dissipation resulting from the drift resonance of trapped particles.<sup>3,5</sup> The diamagnetic effects that we consider here are more robust in that they depend on the gradients of density and temperature in a large volume of the plasma, as opposed to a small inertial layer surrounding the rational surface where gradients could easily be locally flattened.

To implement the eigenvalue system defined by Eqs. (5)–(12) numerically, we have modified the MARS code<sup>17</sup> by decomposing the displacement in two components perpendicular to the equilibrium magnetic field while the third component is replaced by the electrostatic potential. The perturbed quantities are expanded in terms of finite elements in the  $\psi$  direction (with typically  $N_{\psi} = 100$  to 150 elements) and by a Fourier decomposition in the poloidal angle  $\chi$  (typically  $N_{\chi} = 5$  to 10 Fourier components for the circular equilibria treated in this article). Here  $\Delta W_k$  is

evaluated for an assumed eigenvalue  $\omega = \omega_0$  by numerical integration of Eqs. (9) and (10) over pitch angle and energy (typically  $N_{\mu} = 64$  and  $N_{\varepsilon} = 200$ ). The discretized equations are then obtained as the derivatives of the discretized form of  $\Delta W$  with respect to the expansion coefficients for  $\xi$  and  $\Phi$ . The eigenvalue system has the form  $A(\omega)X = 0$ , where  $X$  is the solution vector and  $A$  a square matrix. Because of the kinetic integrals in Eq. (9),  $A$  has a nontrivial dependence on the eigenfrequency  $\omega$  and the eigenvalue is found by Newton iteration. A guess  $\omega_0$  is given for  $\omega$  and the equation is expanded linearly in  $\delta\omega = \omega - \omega_0$

$$\left( A(\omega_0) + \delta\omega \frac{\partial A}{\partial \omega} \right) X = 0, \quad (13)$$

where  $\partial A / \partial \omega$  is obtained by numerical differentiation. Equation (13) is solved for  $\delta\omega$  by the method of inverse vector iteration (which is standard for the MHD eigenvalue problem<sup>17</sup>). The procedure is repeated with  $\omega_0$  replaced by the new value  $\omega_0 + \delta\omega$  until the eigenvalue converges, which typically requires about five iterations.

*Physical parameters and equilibria.* For the numerical computations, we consider isotropic Maxwellian distributions for electrons and ions but allow for nonequal temperatures,  $T_e \neq T_i$ . The electrostatic effects are isolated by explicitly turning the electrostatic potential on and off. In the cases described first, we ignore collisions because the mode has a growth rate or rotation frequency that is much larger than the effective collision frequency.

We have analyzed a sequence of equilibria with circular cross section and aspect ratio  $R/a = 4$ , computed with the CHEASE equilibrium code.<sup>18</sup> In the central  $q < 1$  region, the shear is rather weak:  $q_0 \approx 0.93$  and  $\rho_{q=1} \approx 0.45$  [where  $\rho = (V/V_{\text{tot}})^{1/2}$  is a normalized minor radius and  $V$  is the volume enclosed by a flux surface]. As mentioned in the Introduction, weak central shear makes  $\Delta W_f$  small and consequently the mode becomes more sensitive to non-MHD effects, including those of the trapped particles. The edge  $q$  ranges from 2.3 to 2.6 depending on the pressure and a conducting wall is assumed at 1.2 times the minor radius. The pressure profile has  $dp/d\psi = \text{constant}$  for  $\rho < 0.55$  and is moderately peaked,  $p_0/\langle p \rangle \approx 2.4$ . The equilibria are characterized by their poloidal beta at the  $q=1$  surface,  $\beta_p$ . For this sequence of equilibria, the ideal MHD threshold for the internal kink is  $\beta_{pc} \approx 0.09$ . We consider two sets of physical parameters, termed “small tokamak”:  $B_0 = 1.5$  T,  $R_0 = 0.6$  m, and “large tokamak”:  $B_0 = 3.5$  T,  $R_0 = 3.0$  m. In both cases, the electron density is  $n_e = 2 \times 10^{19} \text{ m}^{-3}$ , and the ions are deuterons. We frequently refer to a “standard” case in which the electron and ion temperatures are equal,  $\eta = 1.5$  and  $\beta_p = 0.4$ , well above the MHD threshold. The profiles of  $I^* = \langle j_{\phi}/R \rangle$ , safety factor  $q$  and plasma pressure  $p$  for the standard case, are shown in Fig. 1. The corresponding peak temperatures are 26 keV for the large and 4.8 keV for the small tokamak cases, respectively, so that the neglect of collisions is well justified.

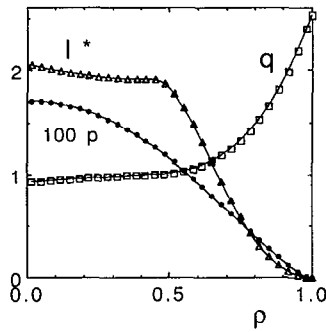


FIG. 1. Radial profiles for pressure, surface averaged toroidal current density, and safety factor for standard equilibrium with  $\beta_p=0.4$ .

To get an overview of how the drift kinetic results connect with the MHD results, we use a multiplier  $f$  for the non-MHD terms in  $\Delta W$ , Eq. (5). The multiplier essentially corresponds to the number of trapped particles;  $f=0$  gives MHD with  $\Gamma=0$ , and  $f=1$  gives the physical trapped particle density. Frequencies and growth rates are given in units of the toroidal Alfvén frequency.

### III. TRAPPED PARTICLE EFFECTS FOR $\Phi=0$

#### A. Stabilization and complex conjugate bifurcation

For simplicity, we first consider nonelectrostatic modes by setting  $\Phi=0$ . Figure 2 shows how the growth rate and rotation frequency of the mode vary with the trapped particle multiplier. The figure applies to the large tokamak parameters and the standard case  $T_e=T_i$ ,  $\eta=1.5$ , and  $\beta_p=0.4$ . A distinct feature is the existence of two branches of eigenvalues: one of which approaches the MHD solution as  $f \rightarrow 0$ , the other emerges with zero growth rate for some positive  $f=f_m$  ( $\approx 0.28$  for this particular case). This occurs at the marginal point for the low frequency energy principle at  $\omega=0$ ,  $\Delta W_{\text{lf}}^{(\omega=0)} = \Delta W_f + f_m \Delta W_k^{(\omega=0)} = 0$ .

Equations (9) and (11) show that for isotropic distributions, all terms not involving  $\Phi$  in  $\Delta W_k^{(\omega=0)}$  [as well as in the Kruskal–Oberman energy principle  $\Delta W_k^{\text{KO}} = \Delta W_k(\omega_*, \langle \omega_d \rangle = 0)$ ] depend on the particle distributions only via the pressure, that is, not on the density and

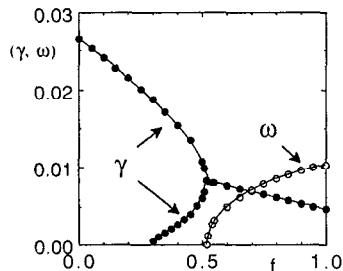


FIG. 2. Growth rate  $\gamma$  and frequency  $\omega$  versus the trapped particle multiplier  $f$  for the standard case  $\beta_p=0.4$  and  $T_e=T_i$  and the electrostatic potential turned off. Note the second branch that does not connect to the MHD mode at  $f=0$ , coalescence, and the formation of a complex conjugate pair.

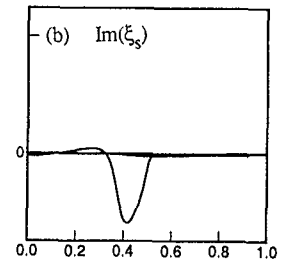
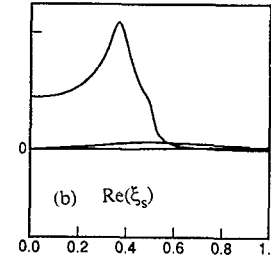
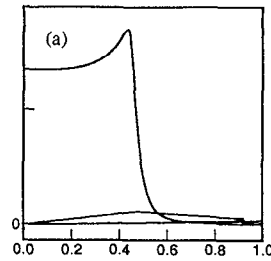


FIG. 3. Fourier components of the normal displacement for two cases in Fig. 2. (a) Second (i.e., non-MHD) branch at  $f=0.35$  with  $\gamma=1.7 \times 10^{-3} \omega_A$ . (b) Rotating branch at  $f=1$  with  $\gamma=5.1 \times 10^{-3} \omega_A$ ,  $\omega=9.8 \times 10^{-3} \omega_A$ .

temperature profiles individually. This implies that the value  $f_m$  where the second branch appears depends only on MHD quantities and not, e.g., on  $\eta$  or  $\omega_*/\omega_A$ . Thus, for isotropic distributions and  $\Phi$  negligible, both the high and low frequency limits of  $\Delta W$  are independent of the density profile. The numerical results for  $\Phi=0$  show that the eigenvalues are very insensitive to  $\eta$ . Furthermore, the dependence on  $\omega_*/\omega_A$  is weak in the sense that the results change little with respect to  $\omega_*/\omega_A$  in the range of densities where tokamaks can be operated.

Figure 2 shows that the MHD branch is stabilized as  $f$  increases, while the second branch is destabilized. In fact, the second branch is stable when  $\Delta W_{\text{lf}}^{(\omega=0)} < 0$  and unstable when  $\Delta W_{\text{lf}}^{(\omega=0)} > 0$ , showing that the zero-frequency energy principle can be both unnecessary and insufficient in the presence of particles with unfavorable drifts. At some intermediate point  $f=f_c$  ( $\approx 0.52$  in Fig. 1) the two branches coalesce and for  $f > f_c$  they form a complex conjugate pair, which remains overstable up to  $f=1$ . (The complex conjugate solution with the opposite rotation frequency is not shown in Fig. 2.) The two rotating branches are related to the fishbone mode. We note that with Maxwellian distributions and  $T_e=T_i$ , these modes become increasingly stable with increasing number of trapped particles.

Figure 3 shows the poloidal Fourier components of the normal displacement [ $\xi_s = \xi \cdot \nabla s$  where  $s = (\psi/\psi_{\text{edge}})^{1/2}$ ] for the second branch at  $f=0.35$  (soon after it emerges) and the unstable rotating mode at  $f=1$ . The displacement for the second branch at  $f=0.35$  is similar to that of the normal MHD internal kink. Thus, the difference between the two branches before the coalescence at  $f \approx 0.52$  is connected with the kinetic rather than the fluid aspects of the mode, i.e., with the frequency dependence of  $\Delta W_k$  and  $K$ .

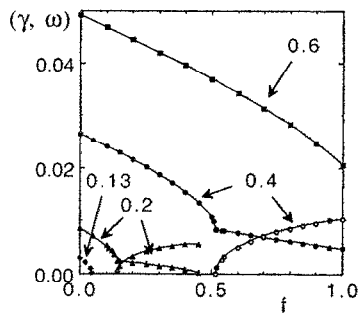


FIG. 4. Eigenvalues vs trapped particle multiplier for different ideal-MHD driving energies. Solid symbols give growth rates and open symbols frequencies. The curves are labeled by  $\beta_p$  at the  $q=1$  surface.

## B. Dependence on MHD driving, drift frequencies, and temperature ratio

In Fig. 2 where  $\beta_p=0.4$ , the physically meaningful case  $f=1$  is overstable. To elucidate the behavior for other parameter values, Fig. 4 shows the eigenvalues versus the trapped particle multiplier for different MHD driving energies  $\beta_p$ . For  $\beta_p=0.13$ , just above the ideal MHD threshold, the mode stabilizes before any bifurcation takes place with very few trapped particles; for  $\beta_p=0.20$ , the mode first bifurcates and then stabilizes with a nonzero frequency at  $f \approx 0.45$  and remains stable up to  $f=1$ ; for  $\beta_p=0.4$  the bifurcation occurs but the mode remains overstable at  $f=1$ . Far above the MHD threshold, at  $\beta_p=0.6$ , the mode remains unstable with a real growth rate for  $f=1$ . Evidently, for this sequence of equilibria (and the large tokamak parameters), the stability threshold in  $\beta_p$  including the trapped particles lies between 0.2 and 0.4. Figure 5 shows the structure of the displacement for a near-marginal case with  $\beta_p=0.2$ ,  $f=0.45$ . The mode approaches the marginal point with a finite rotation frequency ( $\omega/\omega_A \approx 5.6 \times 10^{-3}$ ) and this gives rise to logarithmic singularities at  $q \approx 1 \pm \omega/\omega_A$ , which can be identified in Fig. 5.

Figure 6 shows how the trapped particle effects depend on the ratio of the drift to Alfvén frequencies, which may be seen as a measure of the machine size. The different curves give the growth rates and frequencies versus the

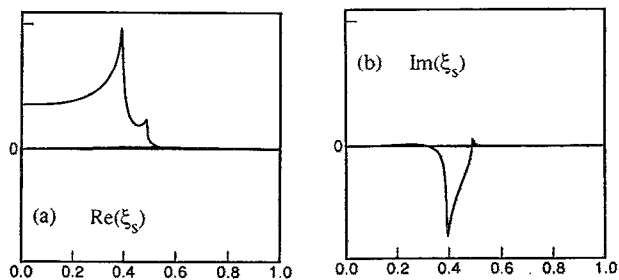


FIG. 5. Fourier components of normal displacement  $\xi_s$  close to marginal stability at  $\beta_p=0.2$ ,  $f=0.47$  with eigenvalue  $\gamma=0.3 \times 10^{-3} \omega_A$ ,  $\omega=5.7 \times 10^{-3} \omega_A$ . Note that  $\xi_s$  approaches a logarithmically singular behavior at  $q=1 \pm \omega/\omega_A$  as  $\gamma \rightarrow 0$ . (a) gives the real and (b) the imaginary part of  $\xi_s$ .

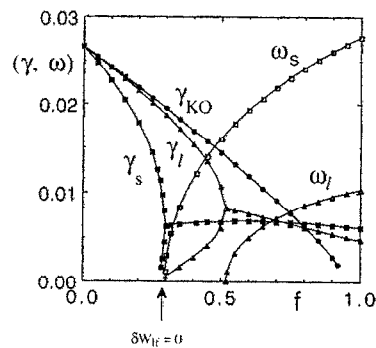


FIG. 6. Bifurcation diagram for different  $\omega_*/\omega_A$  (or different machine size) and the same equilibrium as in Fig. 2 with  $\beta_p=0.4$  and  $T_e=T_i$ . Subscripts on frequencies and growth rates indicate: s—"small", and l—"large" tokamak parameters, and KO—Kruskal-Oberman, or infinitely large tokamak. Note that drift effects are stabilizing when the mode rotation is slow ( $f < 0.7$ ) but becomes destabilizing for faster rotation ( $f > 0.85$ ).

trapped particle multiplier  $f$  for the small and large tokamak parameters, together with the Kruskal-Oberman result (for  $\omega_* = \langle \omega_d \rangle = 0$  corresponding to an infinitely large tokamak). We see that finite  $\omega_*/\omega_A$  is stabilizing when the mode frequency is small ( $f < 0.7$ ) but becomes destabilizing for faster mode rotation ( $f > 0.85$ ). This indicates destabilization by the drift resonance.

The destabilization by the drift resonance is shown more clearly by Fig. 7 for the case of unequal temperatures  $T_i/T_e=3$ ,  $\beta_p=0.4$ , and "small tokamak" parameters. The modes rotating in the electron and ion drift directions now have different growth rates, and the branch rotating in the direction of the hotter species has been destabilized while the other branch has been stabilized in comparison with the equal temperature case in Fig. 2. The destabilization of the ion branch in Fig. 7 by drift resonance is the same type of instability as the fishbone mode. This also applies for the rotating modes in the case of equal temperatures. However, with  $T_i=T_e$ , the growth rate decreases with the trapped particle multiplier.

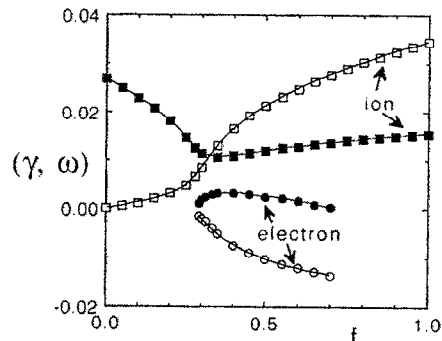


FIG. 7. Asymmetric bifurcation diagram for unequal temperatures  $T_i/T_e=3$  and  $\beta_p=0.4$ . Filled symbols show growth rates and open symbols rotation frequencies. The mode rotating in the direction of the hotter species is destabilized by the drift resonance.

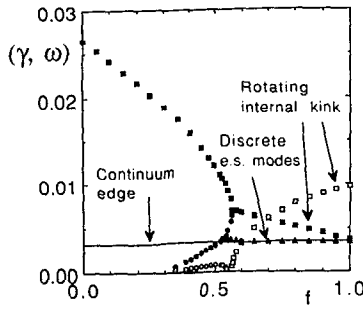


FIG. 8. Frequencies and growth rates versus trapped particle multiplier with electrostatic perturbations included. Growth rates are indicated by solid and frequencies by open symbols. The line marked continuum edge shows that maximum growth rate of the continuum of electrostatic trapped particle modes.

#### IV. MODIFICATIONS FROM THE ELECTROSTATIC POTENTIAL

##### A. Bifurcation diagram

When the electrostatic potential  $\Phi$  is included in Eqs. (4)–(11), a new class of modes appears: the predominantly electrostatic trapped particle modes. (In the limit of zero beta, these are purely electrostatic.) In the present description, which ignores effects of finite banana widths, their growth rates are determined from local conditions on each flux surface and constitute unstable continua. Numerically, these modes appear as delta functions in the electrostatic potential  $\Phi$ , and at finite beta, they couple to electromagnetic perturbations via the pressure. Eigenvalues versus the trapped particle multiplier are shown in Fig. 8 for the standard case and “large tokamak” parameters. By comparing with Fig. 2 we see that  $\Phi$  is stabilizing for the internal kink solution but the effect is weak. The main modification of Fig. 2 is the addition of the unstable continuum of electrostatic modes whose growth rates extend up to the line marked “continuum edge.”

The second electromagnetic branch in Fig. 8 becomes unstable at about the same  $f$  ( $\approx 0.3$ ) as in the nonelectrostatic case. However, with the electrostatic potential included, it splits into a complex conjugate pair with small real frequencies, which separate the pair of discrete modes from the electrostatic continuum. When the growth rate reaches slightly above the continuum edge (by about  $5 \times 10^{-4} \omega_A$ ), the discrete pair bifurcates into two modes with real growth rates: one electromagnetic branch, similar to that in the nonelectrostatic case, and one predominantly electrostatic mode.

The growth rate of this discrete, electrostatic, trapped particle mode remains just above the edge of the continuum, with a separation of a few times  $10^{-4} \omega_A$ . The main feature of the mode is a localized, but continuous,  $\Phi$  perturbation centered around the  $\psi$  surface where the local electrostatic growth rate has a maximum.

##### B. Electrostatic trapped particle modes and their effects on the $q < 1$ region

Although the trapped particle modes predominantly affect the external region, they are of interest for the dy-

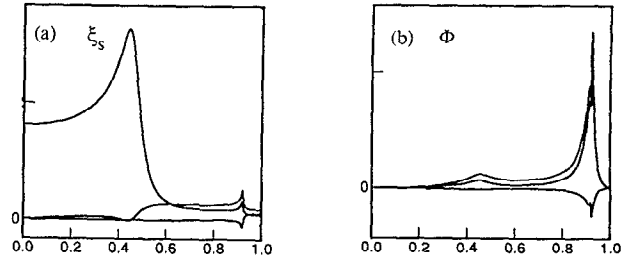


FIG. 9. Mode structure of (a) the normal displacement  $\xi_s$  and (b) the electrostatic potential  $\Phi$  for a discrete coupled trapped particle-internal kink mode at  $\beta_p=0.4$ ,  $f=1$ . The mode growth rate,  $\gamma=3.6 \times 10^{-3} \omega_A$ , is just above the electrostatic continuum.

namics of the central  $q < 1$  region, because they couple to the internal kink mode at finite beta. Examples of such coupled trapped particle-internal kink modes are shown in Figs. 9 and 10 for the standard configuration  $\beta_p=0.4$ ,  $\eta=1.5$  at  $f=1$ . Figure 9 shows the discrete mode at  $\gamma=3.56 \times 10^{-3} \omega_A$ , just above the continuum, and Fig. 10 shows a mode inside the continuum at  $\gamma=3.2 \times 10^{-3} \omega_A$ . The  $\Phi$  perturbation is rather localized in both cases. However,  $\Phi$  is smooth for the regular, discrete mode, but has two delta functionlike peaks for the continuum mode.

The growth rates of the coupled modes are generally very close to the edge of the electrostatic continuum, and their energies are dominated by the  $\Phi$  perturbations which peak far outside the  $q=1$  region. The internal kink part of these modes may be best viewed as a perturbation induced by the trapped particle mode. (A better known example of this kind is the driving of a large amplitude tearing mode by external field errors, when the resistive tearing stability parameter  $\Delta'$  is small and negative.<sup>19</sup>) It does not appear useful to discuss the stability thresholds of the coupled modes. Instead, we consider the size of the internal kink displacement that results from a thermal fluctuation of a trapped particle mode. We assume an electrostatic fluctuation such that  $e\phi_{\max}/T \approx \rho_{Li}/L_n$ , where  $\rho_{Li}$  is the ion Larmor radius and  $L_n$  the density scale length, and use the numerically computed mode structure to obtain the accompanying internal kink displacement. The result is shown in Fig. 11 for the same equilibrium sequence as in Fig. 4, with two different density profiles. One is derived

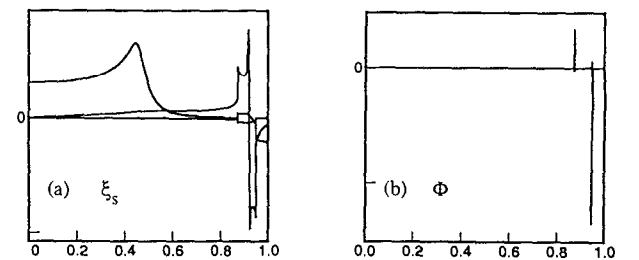


FIG. 10. Mode structure of (a) the normal displacement  $\xi_s$  and (b) the electrostatic potential  $\Phi$  for a singular, coupled trapped particle-internal kink mode at  $\beta_p=0.4$ ,  $f=1$ . The growth rate,  $\gamma=3.2 \times 10^{-3} \omega_A$ , lies within the electrostatic continuum. Note the two sharp spikes in  $\Phi$  at the two radii where the local dispersion relation is satisfied.

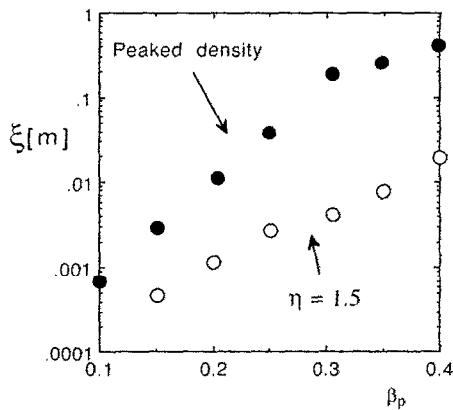


FIG. 11. Central displacement caused by a saturated trapped particle mode for two different density profiles. Note the dramatic increase in displacement with pressure.

from the pressure profile by fixing  $\eta=1.5$ . For this profile, the trapped particles modes peak near  $q=2$ . The other density profile is more peaked,  $n=n_0(1-1.6\rho^2+0.8\rho^4)$ , and the trapped particle modes peak at  $q\approx 1.4$ . As shown by Fig. 11, the displacement can become very large for the peaked density profile. However, the density peaking required to produce this effect is substantial. The  $\eta=1.5$  profile is more typical of tokamaks, and for this profile, the internal kink displacement is significant only at high  $\beta_p$ . A striking feature of Fig. 11 is that the induced internal kink displacement increases very steeply with the pressure. Fluctuations in the position of the central region of the order of 1 mm or somewhat less have been observed<sup>20</sup> in the JET (Joint European Tokamak<sup>21</sup>).

In contrast to the modes discussed previously in this article, the trapped particle modes are sensitive to collisions, because their growth rates are small and the modes localize close to the edge of the plasma where the collision frequency is higher. If collisions are modeled as in Eq. (9b) with the appropriate  $v_{\text{eff}}$ , the local electrostatic growth rate  $\gamma(\psi)$  becomes complex and at low  $\beta_p$ , we can no longer find global electrostatic modes without any radial singularity. As a consequence, the induced kink displacements are considerably decreased by collisions for  $\beta_p < 0.25$ . The present description of the trapped particle modes is clearly too crude to make a precise estimate when the global modes are destroyed by collisions. We believe that the results in Fig. 11 can be taken as an upper limit for the induced displacement.

The results shown in Fig. 11 are of interest for the validity of nonideal boundary layer theories of the internal kink. A well-known difficulty of linear theories, where the stability of global modes is decided by dynamics taking place in thin layers, is the sensitivity to fluctuations. The present calculation gives an explicit estimate of the minimum layer width to consider for the internal kink mode. For  $n_e=2\times 10^{19} \text{ m}^{-3}$  and deuterium ions (with  $R_0/a=4$  and a parabolic pressure profile), the ion Larmor radius is about  $1 \text{ cm} \times \beta_p^{1/2}$ . According to Fig. 11, the displacement induced by thermal electrostatic fluctuations is comparable

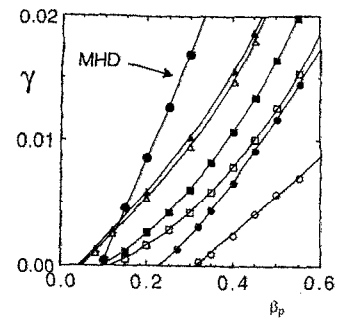


FIG. 12. Growth rates of the electromagnetic mode versus  $\beta_p$  for small tokamak parameters and different assumptions. The MHD result is identified by an arrow and the drift kinetic results are identified as follows: filled symbols give the nonelectrostatic results ( $\Phi$  turned off), open symbols show results with  $\Phi$  included, circles represent  $T_i/T_e=1$ , squares:  $T_i/T_e=1.5$ , and triangles:  $T_i/T_e=3$ .

to the ion Larmor radius when  $\beta_p \approx 0.3$  for the  $\eta=1.5$  profile or  $\beta_p \approx 0.15$  for the more peaked profile.

## V. STABILITY THRESHOLDS

In comparing the present calculations to previous ideal MHD results,<sup>9,10</sup> the most important issue is the stability thresholds with the physical number of trapped particles ( $f=1$ ). We have shown that the thermal trapped particles have strong effects on the internal kink mode and that these effects are mostly stabilizing. (The zero-frequency, coupled trapped particle-internal kink modes discussed in Sec. IV B are disregarded here.) Figure 12 shows growth rates for the ideal internal kink mode versus  $\beta_p$  computed from MHD and drift kinetic theory with several different assumptions: with and without the electrostatic potential  $\Phi$ , and for different temperature ratios  $T_i/T_e$  (all for the "small tokamak" parameters). The ideal-MHD threshold for these equilibria is  $\beta_{pc,\text{MHD}} \approx 0.09$ , and the Kruskal-Oberman energy principle gives  $\beta_{pc,\text{KO}} \approx 0.39$ . The drift kinetic threshold for equal temperatures is below the Kruskal-Oberman result:  $\beta_{pc}=0.32$  ( $\beta_{pc}=0.23$  for the nonelectrostatic calculation  $\Phi=0$ ).

Concerning the effects of unequal temperatures, we note some differences between the drift kinetic and high frequency energy principles. Unequal temperatures are destabilizing in the drift kinetic model but have no effect with the high frequency energy principle. For  $T_i/T_e=1.5$ , the drift kinetic threshold has fallen to  $\beta_{pc}=0.12$  ( $\beta_{pc}=0.10$  with  $\Phi=0$ ) and for  $T_i/T_e=3$ , it is even below the MHD threshold  $\beta_{pc}=0.05$  ( $\beta_{pc}=0.06$  with  $\Phi=0$ ). Thus, the full drift kinetic theory shows destabilization with increasing temperature ratio because of the drift resonance, while the Kruskal-Oberman principle does not show any dependence on the temperature ratio. Furthermore, the Kruskal-Oberman result is not affected by the electrostatic potential, because the magnetic forces affect the particles in such a way that quasineutrality is maintained with  $\Phi=0$ .

The numerical results show a weak stabilizing influence of the electrostatic potential on the *rotating* internal kink modes. This stabilization is strongest for equal tem-



peratures. It appears that for large temperature ratios, the potential is "short circuited" by the colder species which gives a large contribution to  $\rho_\phi$ , see Eq. (8b).

When compared with ideal-MHD, drift kinetic theory predicts strong stabilization by thermal trapped particles if the electron and ion temperatures are about equal. For large temperature ratios, the hotter of the trapped species contributes to destabilize the internal kink by the drift resonance. At sufficient temperature ratios (above about 2 depending on parameters) the drift resonance leads to instability below the ideal-MHD threshold. In this respect and in its physical origin, the instability is similar to the fishbone instability.<sup>1</sup>

## ACKNOWLEDGMENTS

T. M. Antonsen gratefully acknowledges the support of the Centre de Recherches en Physique des Plasmas and the Ecole Polytechnique Fédérale de Lausanne during spring 1992, when this work was started.

This work was partially supported by the Fonds National Suisse de la Recherche Scientifique and the U.S. Department of Energy.

## APPENDIX: LARGE ASPECT RATIO EVALUATION OF $\Delta W_k$

In this appendix, we evaluate  $\Delta W_k$  [Eq. (9)] in a circular, large aspect ratio equilibrium for a standard internal kink displacement:  $\xi_r = \xi \cos(\theta - \phi)$  inside the  $q=1$  surface, and  $\xi_r=0$  outside. The double brackets in Eq. (9a) mean that we divide the spatial integral and multiply the velocity space integral by the same factor  $\int dl/B$  over one poloidal turn. Thus the integration is factored as

$$\int \left( \int \frac{dl}{B} \right)^{-1} d^3x = B \int \frac{r dr}{q} \int d\phi_0 \quad (\text{A1})$$

times

$$\int \frac{dl}{B} \int d\Gamma = \left( \frac{2R}{m} \right)^{3/2} \frac{\pi q}{r^{1/2}} \int_0^\infty \varepsilon^{-1/2} d\varepsilon \times \int_{\varepsilon/B_{\max}}^{\varepsilon/B_{\min}} I_1 d\mu. \quad (\text{A2})$$

In Eq. (A1),  $\phi_0$  is the toroidal angle at which the particle passes the midplane  $\theta=0$ . In Eq. (A2) the poloidal integration has been cast as an orbit integral  $\int dl/v_{||}$  represented by

$$\begin{aligned} I_1 &= \int_{-\theta_t}^{\theta_t} \frac{d\theta}{\sqrt{\cos \theta - \cos \theta_t}}, \\ &= \int_0^1 \frac{2\sqrt{2}dt}{\sqrt{(1-t^2)(1-k^2t^2)}} \\ &= 2\sqrt{2}K(k), \end{aligned} \quad (\text{A3})$$

where  $\theta_t$  is the poloidal angle at the turning point,  $K$  is the complete elliptic integral of the first kind of argument  $k = \sin \theta_t/2$ , and the substitution  $\sin \theta/2 = kt$  was used.

The unperturbed distribution function is given by  $f_0 = n_0(m/2\pi T)^{3/2} \exp(-\varepsilon/T)$  and the large aspect ratio approximation for  $H$  is

$$H = -\frac{\mu B \xi}{R} \langle \cos \theta_0 \rangle \cos \phi_0 \approx -\frac{\varepsilon \xi}{R} \frac{2E(k) - K(k)}{K(k)} \cos \phi_0, \quad (\text{A4})$$

where  $E(k)$  denotes the complete elliptic integral of the second kind. It is convenient to replace  $\varepsilon$  and  $\mu$  by the nondimensional integration variables  $z = \varepsilon T$  and  $k^2$  [with  $d\mu = -(2\varepsilon r/BR)dk^2$ ]. Then, the large aspect ratio expression for  $\Delta W_k$  in Eq. (9) becomes

$$\begin{aligned} \Delta W_k &= 2(2\pi)^{1/2} R \xi^2 \int_0^{\varepsilon_{q=1}} p \varepsilon_r^{3/2} d\varepsilon_r \int_0^\infty z^{5/2} e^{-z} dz \\ &\times \int_0^1 dk^2 \frac{(2E-K)^2}{K} \frac{\omega - \omega_* [1 + \eta(z-3/2)]}{\omega - \langle \omega_d \rangle} \end{aligned} \quad (\text{A5})$$

from which we evaluate the Kruskal-Oberman and zero-frequency limits.

The Kruskal-Oberman limit is obtained by setting  $\omega_* = \langle \omega_d \rangle = 0$ . A straightforward calculation, using  $p \approx p_0 = 2\langle p \rangle = (B^2/4\pi)\beta_p \varepsilon_a^2$  for a parabolic pressure profile gives

$$\Delta W_k^{\text{KO}} \approx \frac{3I_{\text{KO}}}{\sqrt{2}} \beta_p \varepsilon_a^2 \varepsilon_{q=1}^{5/2} R B_0^2 \xi^2 \approx 1.18 \beta_p \varepsilon_a^2 \varepsilon_{q=1}^{5/2} R B_0^2 \xi^2, \quad (\text{A6})$$

where we used the numerical value

$$I_{\text{KO}} = \int_0^1 \left( \frac{(2E-K)^2}{K} \right) dk^2 \approx 0.554 \quad (\text{A7})$$

given in Ref. 6.

For the zero-frequency limit of Eq. (A5), we use  $\mathbf{v}_{dj} = (c\mu/Rq_j)\nabla Z$  and  $\alpha = \phi - q\theta$ , valid for a circular cross section and the lowest order in  $r/R$ . Thus (for a right-handed coordinate system)

$$\begin{aligned} \langle \omega_{dj} \rangle &= \frac{c\mu}{Rq_j} \left( \frac{q}{r} \langle \cos \theta \rangle + \frac{dq}{dr} \langle \theta \sin \theta \rangle \right) \\ &= \frac{c\mu q}{Rr q_j} \frac{2E(k) - K(k) + 2sS(k)}{K(k)}, \end{aligned} \quad (\text{A8})$$

where  $s = rdq/dr$  denotes the shear, and  $S(k)$  is defined as

$$\begin{aligned} \int_{-\theta_t}^{\theta_t} \frac{\theta \sin \theta d\theta}{\sqrt{\cos \theta - \cos \theta_t}} &= 8\sqrt{2}k^2 \int_0^1 \frac{\sqrt{1-t^2}}{\sqrt{1-k^2t^2}} dt \\ &= 4\sqrt{2}S(k) \end{aligned} \quad (\text{A9})$$

[ $S(k)$  can be related to the standard elliptic integrals by  $K(k) = dS/dk^2$ ]. The diamagnetic drift frequency can be written (for  $\eta=0$ ) as  $\omega_{*j} = -(cq/Bq_j n_j r) dp_j/dr$ . Together with Eq. (A8) this gives

$$\frac{\omega_{*j}}{\langle \omega_{dj} \rangle} = -\frac{R}{z p_j} \frac{dp_j}{dr} \frac{K(k)}{2E(k) - K(k) + 2sS(k)}. \quad (\text{A10})$$

For a parabolic pressure profile,  $dp/dr = -(rB^2/2\pi R^2)\beta_p$ , and substitution of Eq. (A10) into Eq. (9) gives

$$\Delta W_k^{(\omega=0)} = \frac{3}{7\sqrt{2}} I_0 \beta_p \epsilon_{q=1}^{7/2} R B_{05}^2 \epsilon^2, \quad (\text{A11})$$

where

$$\begin{aligned} I_0 &= \int_0^1 dk^2 \frac{(2E-K)^2}{2E-K+2sS} \\ &= \int_0^1 (2E-K-2sS) dk^2 + O(s^2). \end{aligned} \quad (\text{A12})$$

The integrals over the elliptic integrals in  $I_0$  can be evaluated by inverting the order of integration, giving  $\int_0^1 K(k) dk^2 = 2$ ,  $\int_0^1 E(k) dk^2 = 4/3$ , and  $\int_0^1 S(k) dk^2 = 8/9$ . Thus, Eq. (A11) becomes

$$\Delta W_k^{(\omega=0)} = \frac{\sqrt{2}}{7} (1 - \frac{8}{3}s + O(s^2)) \beta_p l \epsilon_{q=1}^{7/2} R B_{05}^2 \epsilon^2, \quad (\text{A13})$$

where the shear  $s$  has to be suitably averaged. Thus, the zero-frequency energy principle predicts a stabilizing contribution from the thermal trapped particles of the form in Eq. (3) with the numerical coefficient  $c_{LF} = \sqrt{2}/7 \approx 0.20$ .

It may be noted that there is considerable cancellation of the trapped particle contributions from the regions of favorable and unfavorable curvature in Eq. (A12). In the limit of small shear, the  $\Delta W_k^{(\omega=0)}$  is the average of  $\cos \theta$ , weighted by  $d\mu dl/v_{||}$ :

$$\frac{\int d\mu \int \cos \theta dl/v_{||}}{\int d\mu \int dl/v_{||}} = \frac{\int_0^1 [2E(k) - K(k)] dk^2}{\int_0^1 K(k) dk^2} = \frac{1}{3}.$$

This cancellation indicates that the net result for  $\Delta W_k^{(\omega=0)}$  may be sensitive to various effects, e.g., shaping of the cross section and variation of the aspect ratio. (Both these effects are included in the present formulation, but have not yet been explored.)

More importantly, the above calculation indicates that  $\Delta W_k^{(\omega=0)}$  is not very sensitive to the equilibrium profiles, while they are known to be very important for the MHD stability.<sup>9,10,13</sup> Equation (A12) shows that the trapped particle stabilization is somewhat reduced by positive shear, an effect which is counterbalanced by the strong, opposing tendency in  $\Delta W_f$ . In fact, since  $\Delta W_f$  is roughly propor-

tional to  $1 - q_0$ , one could speculate that the main effect of the trapped particles is to stabilize the MHD driving as long as  $1 - q_0$  is small. Only after  $1 - q_0$  becomes sufficiently large can the MHD terms become large enough to counterbalance the trapped particle stabilization.

Another effect which may be very significant for the kinetic stabilization is the deviation from a Maxwell distribution. A non-Maxwellian energy dependence can already be treated by MARS, while anisotropy would require more significant modifications, including changes to the equilibrium.

<sup>1</sup>L. Chen, R. B. White, and M. N. Rosenbluth, Phys. Rev. Lett. **52**, 1122 (1984).

<sup>2</sup>R. B. White, P. H. Rutherford, P. Colestock, and M. N. Bussac, Phys. Rev. Lett. **60**, 2038 (1988); R. B. White, M. N. Bussac, and F. Romanelli, *ibid.* **62**, 539 (1989).

<sup>3</sup>B. Coppi and F. Porcelli, Phys. Rev. Lett. **57**, 2272 (1986).

<sup>4</sup>C. Z. Cheng, Phys. Fluids B **2**, 1427 (1990).

<sup>5</sup>F. Porcelli, Plasma Phys. Controlled Fusion **33**, 1601 (1991), and references contained therein.

<sup>6</sup>T. M. Antonsen, Jr., B. Lane, and J. J. Ramos, Phys. Fluids **24**, 1465 (1981).

<sup>7</sup>T. M. Antonsen and Y. C. Lee, Phys. Fluids **25**, 132 (1982).

<sup>8</sup>J. W. Van Dam, Y. C. Lee, and M. N. Rosenbluth, Phys. Fluids **25**, 1349 (1982).

<sup>9</sup>M. N. Bussac, R. Pellat, D. Edery, and J. L. Soulé, Phys. Rev. Lett. **35**, 1638 (1975).

<sup>10</sup>H. Lütjens, A. Bondeson, and G. Vlad, Nucl. Fusion **32**, 1625 (1992).

<sup>11</sup>R. C. Wolf, J. O'Rourke, A. W. Edwards, and M. von Hellerman, Nucl. Fusion **33**, 663 (1993), and references therein.

<sup>12</sup>B. B. Kadomtsev, Sov. J. Plasma Phys. **1**, 389 (1975) [Fiz. Plasmy **1**, 710 (1975)].

<sup>13</sup>A. Bondeson, G. Vlad, and H. Lütjens, Phys. Fluids B **4**, 1899 (1992).

<sup>14</sup>R. J. Hastie and T. C. Hender, Nucl. Fusion **28**, 585 (1988).

<sup>15</sup>M. D. Kruskal and C. R. Oberman, Phys. Fluids **1**, 275 (1958).

<sup>16</sup>J. W. Connor and R. J. Hastie, Phys. Rev. Lett. **33**, 202 (1974); Phys. Fluids **19**, 1727 (1976).

<sup>17</sup>A. Bondeson, G. Vlad, and H. Lütjens, in *Advances in Simulation and Modeling of Thermonuclear Plasmas*, in Proceedings of the International Atomic Energy Agency Technical Committee Meeting, June 1992, Montréal (International Atomic Energy Agency, Vienna 1993), p. 306.

<sup>18</sup>H. Lütjens, A. Bondeson, and A. Roy, Comput. Phys. Commun. **69**, 287 (1992).

<sup>19</sup>A. H. Reiman, Phys. Fluids B **3**, 2617 (1991).

<sup>20</sup>P. A. Duperrex, A. Pochelon, A. W. Edwards, and J. A. Snipes, Nucl. Fusion **32**, 1161 (1992).

<sup>21</sup>P. H. Rebut and the JET team, in *Plasma Physics and Controlled Nuclear Fusion Research, 1986*. Proceedings of the 11th International Conference, Kyoto (International Atomic Energy Agency, Vienna, 1987), Vol. 1, p. 31.